

Lanthanide Ions Sensitization by Small Noble Metal Nanoclusters

Mirko Vanzan, Tiziana Cesca,* Boris Kalinic, Chiara Maurizio, Giovanni Mattei, and Stefano Corni*

Cite This: *ACS Photonics* 2021, 8, 1364–1376

Read Online

ACCESS |



Metrics & More

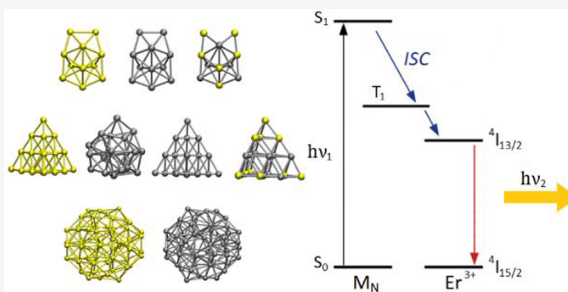


Article Recommendations



Supporting Information

ABSTRACT: Rare-earth ions sensitization is, nowadays, a relevant topic in modern technologies. Noble metal nanoclusters can effectively sensitize lanthanide photoluminescence (PL) via excitation energy transfer (EET). Recent experimental works reported how this process strongly depends on the nanoclusters size and composition, however, a comprehensive understanding of this phenomenon is still lacking. Inspired by the current paradigm on the lanthanide–antenna complexes, where light is absorbed by the organic ligand, which then converts to a triplet and transfers the excitation to the lanthanide, we propose it also applies to sensitization by metal clusters. To prove this, we studied the optoelectronic features of several M_N nanoclusters ($M = \text{Au}, \text{Ag}, \text{Au/Ag mix}$; $N = 12, 20$, and 58) at the Time Dependent Density Functional Theory (TDDFT) level, including, via simplified models, the silica matrix and its possible defects, and make considerations on the role these features can have on the EET toward Er^{3+} ions. Our analysis suggests that PL enhancement is generally more effective when $N = 12$ and $M = \text{Ag}$ or Au/Ag mix , while the worst cases are obtained when $M = \text{Au}$ and $N = 58$. These findings are coherent with prior experimental data and with novel measures that are here presented for the first time. Notably, we recover that the matrix defects can actively take part in the EET and, in some cases, could be (counterintuitively) beneficial for the process efficiency. Globally, this theoretical framework gives a comprehensive rationale that can guide the design of new effective rare-earth ion sensitizers based on metal clusters.



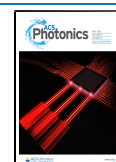
KEYWORDS: photoluminescence, nanophotonics, energy transfer, lanthanide, nanoclusters, metal nanoclusters, rare-earth sensitization

In the past years, the study of the optical activity of rare-earth ions has become a relevant topic in the scientific community.^{1,2} The reason for such widespread interest resides in the sharp and stable emission that these ions present in the visible and near-IR spectral regions. This peculiar capability makes them fundamental actors in optoelectronic applications such as chemical sensors,³ waveguides,⁴ fiber lasers,⁵ and light-emitting diodes (LEDs).⁶ A key-role in modern technologies is played by Er^{3+} ions since they present a major emission band, corresponding to the $^4I_{13/2} \rightarrow ^4I_{15/2}$ transition at $1.54 \mu\text{m}$, which is exactly where standard silica glasses have their absorption minimum. For this reason, these ions can be effectively employed in applications such as optical fibers and nanocomposite glasses.^{7,8} However, erbium ions suffer from two main problems: they have a poor excitation cross-section ($\sigma \approx 10^{-21} \text{ cm}^2$) and they are usually affected by important quenching processes, even at low concentrations.^{9,10} As a consequence, the Er^{3+} photoluminescent (PL) emission is suppressed and the devices performances decrease. From the early 2000s, many efforts were spent in order to increase the emission quantum yield of erbium ions embedded in silica glasses, especially by including in the system sensitizers such as other rare-earth ions,^{11,12} silicon nanocrystals,^{13,14} plasmonic systems,^{15,16} or metallic nanoclusters (NCs).^{16–20} The latter approach seems to be particularly promising since it was proved that even a small amount of metallic atoms, upon

aggregation, can increase the Er^{3+} PL by a factor of 10 or more.^{19,21–24} Given the ultrasmall dimensions of these structures (less than 2 nm), the PL enhancement cannot be related to the plasmonic enhancement of the incoming electric field. The mechanism was demonstrated to be a nonradiative, short-range process between the metallic clusters and the Er^{3+} ions.^{25,26} A possible explanation of this phenomenon can be given by considering the presence of excitation energy transfer (EET) processes that can take place from the metallic aggregates to the Er^{3+} ions. Such a mechanism is well-known in the organic chemistry community as the “antenna–lanthanide” effect.²⁷ When an organic–lanthanide complex interacts with a proper electromagnetic field, the beam can be first absorbed by the organic “antenna”, which generates a localized singlet excited state. Then by intersystem crossing, this singlet excited state might turn into a less energetic and long-living triplet state that can couple with one of the lanthanide excited states. If the coupling is strong enough, the excitation can be transferred to the lanthanide ion, which in

Received: December 11, 2020

Published: May 3, 2021



turn relaxes to a radiative level and then emits at its peculiar wavelength.²⁸ This results in an enhanced emission by the lanthanide atoms, stimulated by the absorption of the antenna. Such paradigm can be applied to the NC-erbium case, considering the NC as the antenna. It is indeed well-known that, once excited, ultrasmall noble-metal systems can undergo a singlet–triplet intersystem crossing due to the strong spin–orbit coupling arising from the high mass of the metal atoms.^{29–34} However, different NCs enhance the Er^{3+} PL in different ways. This can be seen, for example, by the PL emission results for NCs with $N \approx 10$ –15 atoms reported in Figure 1.

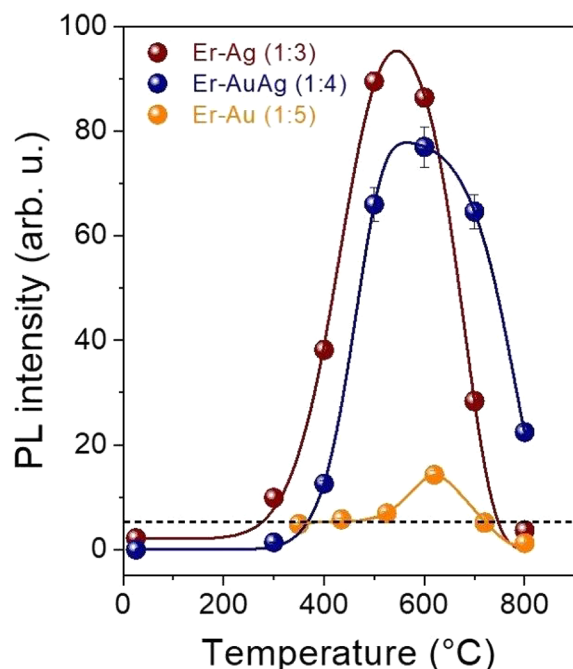


Figure 1. PL intensity of the $\text{Er}^{3+}I_{13/2} \rightarrow {}^4I_{15/2}$ transition as a function of samples annealing temperature of various Er-NC coimplanted silica samples, thermally treated in a N_2 atmosphere. Au, Ag, and AuAg refer to NCs composed of gold, silver, and gold/silver alloy, respectively.^{19,23,35} Ratio within rounded brackets refers to the relative Er-metal implantation fluence in the sample (the Er implantation fluence was about 7×10^{14} at/cm²). The solid lines are to be used as a guide for the eye. The black dashed line indicates the PL emission intensity of the reference sample (Er-implanted silica sample, annealed at 800 °C for 1 h in a N_2 atmosphere). The PL measurements have been taken with excitation at 488 nm, resonant with the ${}^4I_{15/2} \rightarrow {}^4F_{7/2}$ Er^{3+} transition.

Taking into account nanosystems composed of Ag and Au, the main experimental findings coming from PL measurements can be summarized in the following points:

- Ag-based^{24,35} and Au/Ag alloy-based NCs²³ can enhance Er^{3+} PL more effectively than Au NCs (see Figure 1).^{19,22,25,26}
- In the case of Au_N , structures composed by $N = 10$ –15 atoms enhance the lanthanide PL more effectively than larger or smaller aggregates.^{19,36} The optimal size tends to increase (to $N = 20$ –25) when higher Au fluence is used, with a lower estimated enhancement factor.²²
- Small Au_N aggregates ($N = 5$ –10) can increase the PL more effectively if the samples are annealed in a reducing atmosphere, compared to the samples annealed in an

inert atmosphere.³⁷ The opposite occurs instead for Au_N aggregates, with $N = 20$ –25 atoms, for which annealing treatments in a reducing atmosphere, in the temperature region of maximum efficiency (around 600 °C), give rise to a lower Er^{3+} PL enhancement with respect to treatments in an inert atmosphere.²²

The aim of this work is to understand how the features of the NC antenna can affect the EET capabilities and thus the global Er^{3+} PL enhancement. In particular, we want to verify if the aforementioned experimental evidence can be rationalized in an antenna–lanthanide theoretical framework. To do that, we applied Density Functional Theory (DFT) and Time Dependent Density Functional Theory (TDDFT) on various noble-metal NCs, which differ in size, shape, and chemical nature. Although the complex interplay between the SiO_2 matrix and the NCs is not expected to produce size-controlled NCs,^{38,39} we selected specific shapes from the available optimized ones in vacuum. Their structures are reported in Figure 2. The effect of the dielectric silica matrix was modeled in the computational setup, as well as the possible presence of matrix defects.

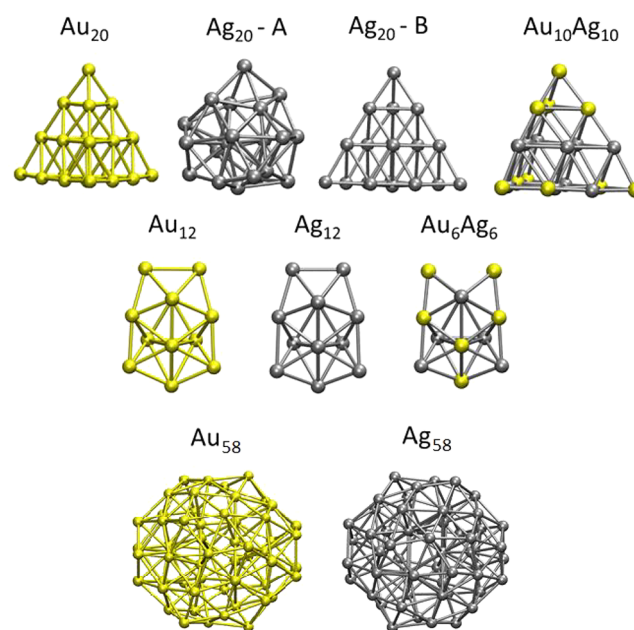


Figure 2. Graphical representation of the investigated nanoclusters. Au atoms are colored in yellow and Ag in gray.

Through these calculations we were able to compare the first triplet excited state (T_1) energy levels of the nanostructures with the emitting ${}^4I_{13/2}$ level of Er^{3+} and to make qualitative considerations on the effectiveness of the T_1 to ${}^4I_{13/2}$ EET process.³⁰ Additionally, we investigated the role the NCs optical activity can have on the excited states populations and, thus, on the EET rate. Moreover, the impact the excited state geometry relaxation can have on the EET yield and thus on the whole PL enhancement is discussed. Notwithstanding the complexity of the experimental systems compared to the computational setup, our calculations return a coherent theoretical framework and provide a rational for the available literature data within the antenna–lanthanide paradigm. Remarkably, our theoretical approach also allowed us to predict the effect a reducing atmosphere annealing could have

on erbium-doped silica samples, sensitized by small Ag_N aggregates ($N = 10\text{--}15$). Such a prediction was then validated against novel experimental results that are here presented for the first time.

■ COMPUTATIONAL METHODS

Nanoclusters' Geometries and Modeling of Defects.

We investigated the T_1 energy level distribution of various noble metal nanostructures considering three main families of NCs: M_{12} , M_{20} , and M_{58} with $M = \text{Au}$, Ag , or a mix of these elements. The structures we considered were chosen on the basis of the information we have on the nanocluster's size under typical experimental conditions, where the sizes for M_N can be divided in three main groups, namely, $N = 10\text{--}15$, $20\text{--}25$, and $50\text{--}60$.^{19,22,24–26,35–37} Therefore, to properly model such structures, we chose a representative cluster within each of these size ranges. The initial geometries of these systems were adapted from the available literature data. Unfortunately, the precise equilibrium structures of these systems are generally unknown. Most of the available data indeed refers to capped structures in which the metal kernel is protected by organic ligands.^{40,41} Therefore, we decided to adopt the experimentally determined structure when available, while relying on previous ab initio calculations in the other cases. Notice that the chosen nanostructure sizes are not always the ones most stable in vacuum, which indeed are typically M_{13} , M_{19} , and M_{55} (even if there are some exceptions, such as Au_{20}).^{42,43} However, given the complex nature of the system, an atomistic insight on the NCs geometries within the experimental setups is not feasible. We thus have to rely on Extended X-ray Absorption Fine Structure Spectroscopy (EXAFS) and X-ray Absorption Near-Edge Structure (XANES) measurements, whose uncertainty in the estimation of the number of the atoms owned by a nanocluster can reach up to the 20–25%.³⁶ Therefore, given the arbitrariness in the choice of some model structures within this interval, we accounted for the specific geometries reported in Figure 2 based on the following reasons: the sizes are compatible with the experimental data, the structures were proved to be energetically stable by previous DFT calculations, and they are constituted by even numbers of atoms, which makes them closed-shell systems and thus computationally more affordable. Moreover, we considered the specific 1:1 alloy composition to investigate the property of systems whose composition is intermediate between the pure metal clusters, in line with experimental mixed clusters having formula $\text{Au}_x\text{Ag}_{1-x}$, $x = 0.6 \pm 0.1$ ²³ (see Supporting Information for more details). We further explored a 1:4 composition for a specific case, analyzing the tetrahedral $\text{Au}_4\text{Ag}_{16}$ nanocluster that was previously discussed in the literature.⁴⁴ In such a structure indeed, there are no Au–Au covalent bonds, and this gives them particular electron transfer properties, as we discuss in the Supporting Information.⁴⁴ Regarding the M_{12} case, we proceeded by selecting the most stable isomer of Ag_{12} reported in ref 45 and modified the atom nature to obtain Au_{12} . To build the 1:1 Au_6Ag_6 alloy, we adapted the Ag_{12} geometry following the spatial arrangement of the atoms presented in ref 46. Regarding M_{20} , we took the starting geometries from Nhat and Tai⁴⁷ who extensively analyzed the relative stability of several M_{20} isomers. From this work we extracted the Au_{20} and $\text{Ag}_{20}\text{-A}$ structures as the most stable isomers obtained from their calculations. In the case of tetrahedral Au_{20} , this structure was experimentally proven to be the most stable in the gas

phase.⁴³ In order to analyze the effect the cluster geometries can have on the PL rate, we studied the energy level distribution of a silver nanostructure having an Au_{20} -like tetrahedral shape. This model was named $\text{Ag}_{20}\text{-B}$. The $\text{Au}_{10}\text{Ag}_{10}$ nanoalloy geometry was based on the lowest energy isomer presented in ref 48. Finally, the M_{58} clusters were obtained by adapting the Au_{58} equilibrium structure presented in ref 49. All the aforementioned NCs are pictured in Figure 2. We also considered the presence of matrix defects. To keep the model as simple as possible, we modeled this defect using an H_3SiO_4^- anion that was placed at 3.5 Å from the NC and was left free to move during the geometry optimization. To explore how sensitive our nanosystems are to the defects, we placed the anion in two different orientations, one with the unsaturated Si–O bond pointing toward a NC face and one with the unsaturated Si–O bond pointing toward a NC edge, see insets of Figures 3 and 5 as examples. Finally, since some of the chosen M_{12} nanostructures do not represent the lowest energy isomer in the gas phase, which have indeed a planar structure,^{42,50} we thus extended our analysis to M_{12} planar structures, investigating also the relative cluster stabilities on the basis of the cohesive energy. The results are available in the Supporting Information.

Computational Details. M_{12} and M_{20} structures were optimized using the hybrid functional B3LYP, together with the LANL2DZ relativistic corrected pseudopotentials and basis sets⁵¹ for the metal atoms, and the 6-31+G* basis set for the atoms modeling the defect. The reliability of this computational level was previously validated in other studies on small metal-based NCs.^{52–55} Because of convergency issues connected to the ab initio optimization of M_{58} systems, they were optimized using the semiempirical PM7 approach, whose accuracy in determining the geometries of metallic nanoclusters was recently tested.⁵⁶ The T_1 energy levels and the bright excitations were computed at the equilibrium geometries in a linear response TDDFT framework, using the aforementioned exchange-correlation functional and basis set. To test the capability of the PM7 technique in calculating optimized structures with proper excited state level locations, we repeated the same procedure for the smaller clusters. The results are summarized in the Supporting Information, page S7. CAM-B3LYP exchange-correlation functional was also employed to test how the calculation level can affect the geometries and the location of the T_1 levels for the M_{12} cases. Geometry optimization of T_1 excited states was performed by imposing a spin multiplicity of 3 to the ground state electronic structures. All calculations were carried out using the Gaussian 09 package.⁵⁷ UV–vis spectra convolution was performed with GaussSum03,⁵⁸ using a width at half-maximum of 0.12 eV. In all calculations, the silica matrix was accounted using the IEFPCM solvation model.⁵⁹ The static dielectric constant and the refractive index were set to 3.9 and 1.46, respectively, which are the common values used for SiO_2 .⁶⁰

■ EXPERIMENTAL METHODS

Ion Implantation and Nanoclusters Formation. Er–Ag coimplanted samples were produced by sequential ion beam implantation of Er and Ag into pure silica slabs (Herasil by Haereus). In order to obtain an almost flat concentration profile of the implanted species, a three-energy implantation scheme was adopted both for Er and Ag and the implantation energies were set in order to get the complete overlap of the

implantation profiles in the coimplanted samples. As the first step, Er was implanted into a pristine silica slab (at 50, 100, and 190 keV) at a total fluence of 8.5×10^{14} at/cm² (measured by Rutherford backscattering spectrometry, RBS). An almost flat concentration profile, about 70 nm thick, centered 60 nm below the slab surface, was obtained. The Er-doped silica slab was then annealed at 800 °C for 1 h in a N₂ atmosphere to recover the implantation damage and to restore the Er–O octahedral coordination, necessary for the Er³⁺ luminescence activation. A piece of this slab was used as the reference sample (named Er800). Subsequently, Ag was implanted into the Er-doped slab (at 45, 80, and 140 keV) at a total fluence of 2.5×10^{15} at/cm² (measured by RBS), corresponding to an [Er]/[Ag] concentration ratio of 1/3. At last, the Er–Ag coimplanted slab was divided in two, and two sets of samples were produced by making isochronal (1 h) thermal annealing treatments at incremental temperatures in the range 300–800 °C in inert (N₂) and reducing (Ar + H₂) atmospheres. The thermal treatments are necessary to further recover the implantation damage and induce the Er³⁺ luminescence activation and to promote the formation of Ag_N clusters in the silica matrix.

Photoluminescence Measurements. Photoluminescence (PL) measurements were performed at room temperature by exciting the samples with a multiline Ar laser, mechanically chopped at 6 Hz. Different laser lines can be selected by interference filters. In this case, the 488 nm line was used to get the resonant excitation of the Er³⁺ ions in the samples (in resonance with the $^4I_{15/2} \rightarrow ^4F_{7/2}$ Er³⁺ absorption transition). The PL emission was spectrally selected by a single-grating monochromator and detected by a N₂-cooled photomultiplier tube (Hamamatsu R5509–72) coupled with a lock-in amplifier.

RESULTS AND DISCUSSION

In this section we will present the main results coming from our calculations. We divided this section in four parts. At first we will show the results obtained for the M_{12} ($M = \text{Au}, \text{Ag}, \text{Au/Ag alloy}$) NCs, focusing on the analysis of T_1 energy level distributions and on the absorption features. Then we will present and discuss the data obtained for the M_{20} ($M = \text{Au}, \text{Ag}, \text{Au/Ag alloy}$) systems. After that, we will briefly discuss the results obtained for the M_{58} ($M = \text{Au}, \text{Ag}$) structures, and last, we will cover the role the excited state geometry relaxation can have on the EET process.

Since we are trying to interpret the experimental findings in a unique and coherent theoretical framework, we have to take into account the conditions in which the experiments were conducted. Most of the measurements we will refer to were conducted on Er³⁺-doped silica glasses where the NCs were incorporated by ion implantation. Therefore, we decided to include in our calculations the effect of the SiO₂ environment through an implicit model.⁵⁹ With this approach, we were able to account for the effect of the matrix by considering our systems surrounded by a continuum, homogeneous, and isotropic dielectric material, whose dielectric constant and refractive index are the ones of pure silica.⁶⁰ Furthermore, since the ion beam can damage the structure of the dielectric matrix, we extended our calculations to systems where matrix defects are included in the form of an explicit H₃SiO₄[−] anion, whose dangling bond points toward the nanosystem. This anion represents the minimum defect unit with which a NC can interact and modify its EET capabilities. We will now refer

to the calculations performed on the metal NC itself with the name PURE, while we will refer to the calculations that explicitly include the defect with the names FACE and TOP if the Si–O dangling bond of the anion points toward a nanocluster's face or top vertex, respectively. See the [Computational Methods](#) for more details. These two defect locations are local energy minima, but we did not characterize the global energy minimum for the defect position. In fact, we chose the TOP and FACE configurations as limit cases for the defected system (where the defect is interacting with either the least coordinated, TOP, or the most coordinated, FACE, metal atom in the cluster). As such, when both defects yield the same T_1 energy trend compared to the PURE structure, it is reasonable to assume that this trend is representative of what may happen in the defective silica matrix as well.

M_{12} ($M = \text{Au}, \text{Ag}, \text{Au/Ag Alloy}$). The T_1 energy level distribution of the three M_{12} structures are pictured in [Figure 3](#), while their numerical values are reported in [Table 1](#). From

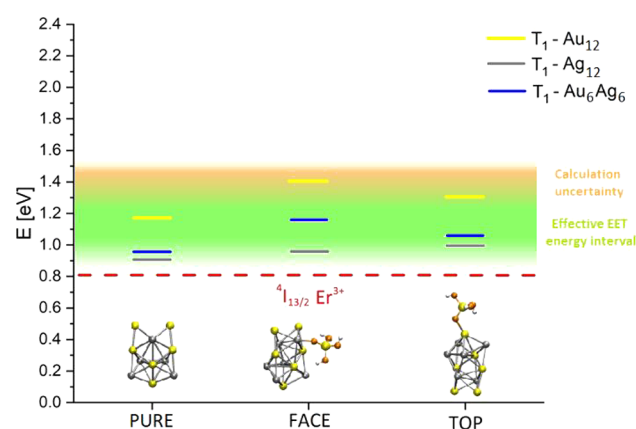


Figure 3. T_1 level distribution of the M_{12} structures. The label PURE indicates results for the bare NCs, while FACE and TOP refer to systems where the matrix defect points to a NCs face and top vertex, respectively. Red line represents the energy of $^4I_{13/2}$ Er³⁺ emitting level (0.81 eV).⁶¹ The green band indicates the region where the EET process is more effective,⁶² while the orange band extends this region, taking into account the uncertainty coming from the chosen calculation level.⁶³ Insets represent the optimized structures of Au₆Ag₆ aggregates.

these data we can see how the silver-based NCs have the lowest T_1 levels, with their energies spreading from 0.89 to 0.99 eV in the case of PURE and TOP defected forms, respectively. On the contrary, Au₁₂ have the highest T_1 levels, whose energies go from 1.17 eV (PURE case) to 1.41 eV (FACE case). The alloy presents an intermediate profile, with the T_1 energies going from 0.95 to 1.16 eV for the PURE and FACE forms, respectively. Such different behaviors arise only from the different chemical nature of the systems, since the starting coordinates adopted during the geometry optimization procedure were the same (see the [Computational Methods](#) for details). This trend suggests that gold structures not only have the most energetic T_1 levels, but also that they are more sensitive to the presence of matrix defects. Indeed, by comparing the T_1 energies of PURE and the defected forms, we recover a PURE to FACE blueshift of about 0.24, 0.07, and 0.21 eV for Au₁₂, Ag₁₂, and Au₆Ag₆, respectively; while comparing the PURE to TOP levels, we recover 0.14, 0.10, and 0.11 eV blueshifts for Au₁₂, Ag₁₂, and Au₆Ag₆, respectively. The total energy differences between the FACE and TOP isomers

are very small (always lower than 0.18 eV), meaning that, in realistic conditions, there would be a comparable number of face and edge defected NCs. In this stage of the analysis we further investigated the role the atoms arrangement can have on the Au₆Ag₆ nanoalloy by swapping Au and Ag atoms both in the pure and defected structures. The swapped NCs are less stable and have more distorted geometries compared to the original; more details are available in the [Supporting Information](#).

As mentioned, the three M_{12} structures were obtained, adapting the same starting coordinates, which are the ones presented in ref 45, for Ag₁₂. In order to explore how the aggregate geometry can affect the T_1 levels distributions, we performed the calculations on the two known most stable isomers of Au₁₂ and Au₆Ag₆ NCs, which will be now called Au₁₂-B and Au₆Ag₆-B.^{46,50} Those structures are profoundly different compared to the ones analyzed until this point, since they are characterized by planar geometries. Our calculations show that Au₁₂-B has its T_1 levels located at 0.75 eV, while Au₆Ag₆-B has it located at 1.02 eV. This indicates that the geometry has a prominent role in determining the electronic properties and thus EET features of the systems, which can be dramatically different considering two different isomers. In particular, Au₁₂-B T_1 level has an energy that is even lower than the Er³⁺ acceptor level, making the EET theoretically forbidden. Despite the fact that these species are the lowest-energy configurations in vacuo, as confirmed by the cohesive energy analysis reported in the [Supporting Information](#), they may not be the most stable geometries in a silica implanted sample, since the matrix surface energy can have a pivotal role in determining the most stable NC geometries.

Because of the planar geometries, these NCs would have a larger exposed surface and would require a higher amount of free energy to be hosted by the matrix compared to the three-dimensional isomers. Considering the surface tension of pure silica⁶⁴ and the relative stabilities of the NCs, we estimated that Au₁₂-B and Au₆Ag₆-B would require extra free energy with respect to their analyzed three-dimensional counterpart of about 0.22 and 0.55 eV, respectively, making their presence less probable in the experimental samples. More details are available in the [Supporting Information](#).

From the photophysics of lanthanide complexes, we know that there is an optimal energy difference between the antenna T_1 level and the acceptor level. This difference is strongly system-dependent and cannot be accurately determined a priori. However, there are some empirical rules that are commonly adopted to design highly luminescent antenna–lanthanide complexes. In particular, much evidence suggests that the energy difference between the donor and the acceptor levels has to be smaller than 0.43 eV (3500 cm^{−1}),²⁸ but greater than 0.23 eV (1850 cm^{−1}), otherwise, the back-energy transfer process would successfully compete with the direct EET.⁶² Thus, considering the $^4I_{13/2}$ of Er³⁺ as the accepting (and emitting) level, whose energy in SiO₂ is about 0.81 eV (1.54 μm),⁶¹ our optimal interval spreads from 1.04 to 1.24 eV. This interval is represented by the green band lines in [Figure 3](#). In this fashion, it can be stated that Au₁₂ and the 1:1 Au/Ag nanoalloy have the best T_1 energies, in the latter case especially when defects are accounted for. This result, however, may suffer from the uncertainty given by the B3LYP exchange–correlation functional in determining the energies of the triplet states. Indeed, despite this functional being one of the best performers in this sense, it tends to underestimate⁶³ the

energies of the excited states of about 0.24 eV, with a mean absolute error of about 0.34 eV.⁶⁵ Such uncertainty is represented by the orange band in [Figure 3](#). Considering this shift, the cases involving Ag₁₂ NCs would now become highly performing since their T_1 falls within the EET optimal energy region and can effectively couple with the $^4I_{13/2}$ Er³⁺ state. In the theoretical framework we are testing, the incoming radiation is first absorbed by the NC antenna and then transferred to the lanthanide. In this view, the EET rate strongly depends on the population of T_1 that, in turn, is directly connected to the population of the optically active excited states. In particular, we can expect that the more the NC absorbs, the more populated would be its T_1 level and the more effective would be the EET process. Searching for a further mechanism that may explain the better sensitizer performances of Ag compared to Au, we investigated the optical absorption of the investigated M_{12} aggregates by calculating their UV–vis spectra (reported in [Figure 4](#)). No

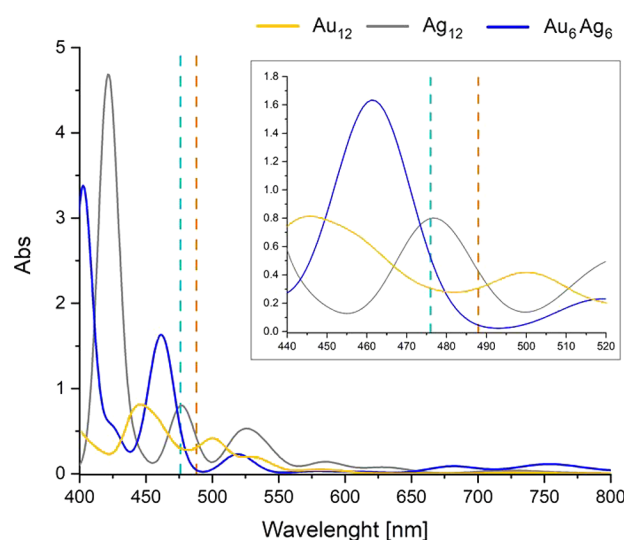


Figure 4. TDDFT-computed absorption spectra for the investigated M_{12} NCs. The inset shows a zoom over the 440–520 nm region. Light-blue and orange dashed lines represent the out-of-resonance (476 nm) and in-resonance (488 nm) wavelengths, respectively, which are commonly adopted to excite the systems in the experimental setups.^{19,22–26}

relative normalization was performed in order to highlight the differences in terms of absorption intensities. We want to focus our comparison to the wavelength at which experimental measurements were done. The available experimental data recovered on Er³⁺-doped glasses were obtained with two main exciting wavelengths: the in-resonance $\lambda = 488$ nm (resonant with the $^4I_{15/2} \rightarrow ^4F_{7/2}$ Er³⁺ transition) and the out-of-resonance $\lambda = 476$ nm radiations.^{19,22–26} We thus focus our analysis in this specific wavelengths interval, highlighted by the dashed orange and the light-blue lines in [Figure 4](#). By looking at the energy interval of interest (around 476 and 488 nm), we can see how Ag₁₂ presents a very intense peak, with its maximum located at 478 nm. Gold NCs seem to absorb less and more uniformly in this region, while the nanoalloy is active at lower wavelengths. The role of matrix defects was studied on the optimized NC-H₃SiO₄[−] TOP geometries. The absorption tendencies are similar to the ones reported in [Figure 4](#) but for the absorption intensities, which are here suppressed by the

presence of charge-transfer states between the anion and the NCs. See [Supporting Information](#) for more details.

Since the H_3SiO_4^- anion is a charged species, there could take place some charge transfer phenomena between the defect and the NCs, which could affect the excited states electronic structure.

This was confirmed by an estimation of the nanocluster's partial charges on the basis of Mulliken population analysis reported in the [Supporting Information](#). Therefore, to explore how such charge transfer effects can modify the energy levels distribution, we performed additional calculations using the long-range corrected CAM-B3LYP functional on the M_{12} PURE and TOP cases. We applied this method both on the B3LYP and on the CAM-B3LYP optimized geometries. Despite the presence of electronic displacement among the NCs and the H_3SiO_4^- anion demonstrated by the Mulliken population analysis, using such an exchange-correlation functional affects the bare and defected NCs in a similar, negligible way; T_1 blueshifts by 0.03 eV (PURE Au_{12} case) to 0.11 eV (TOP Au_6Ag_6 case). These results are reported in the [Supporting Information](#). To summarize, we found that, among the M_{12} systems, the Au_{12} and the Au/Ag nanoalloy have the best T_1 to $^4\text{I}_{13/2} \text{Er}^{3+}$ energy match. However, when the B3LYP underestimation of T_1 levels is taken into account, Ag_{12} resulted in the best performing system in this sense. Moreover, Ag_{12} presents the highest absorption intensity in the excitation window of interest, followed by the gold-based system and the nanoalloy.

M_{20} ($M = \text{Au}, \text{Ag}, \text{Au/Ag Alloy}$). The T_1 energy level distribution of the analyzed M_{20} structures is reported in [Figure 5](#). All energies are reported in [Table 1](#). In all the cases, $\text{Ag}_{20}\text{-A}$

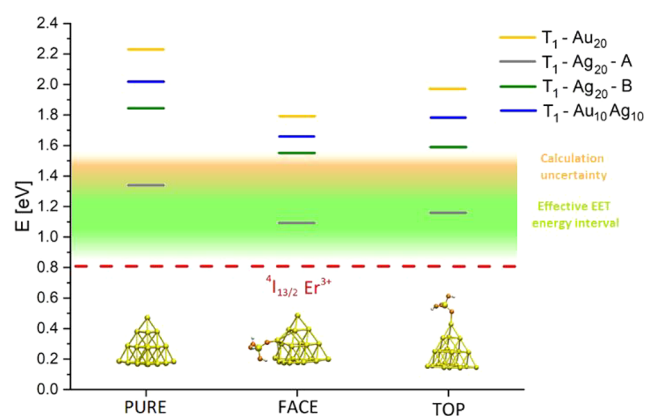


Figure 5. T_1 level distribution of the M_{20} structures. The label PURE indicates results for the bare NCs, while FACE and TOP refer to systems where the matrix defect points to a NCs face and top vertex, respectively. Red line represents the energy of the $^4\text{I}_{13/2} \text{Er}^{3+}$ emitting level (0.81 eV).⁶¹ The green band indicates the region where the EET process is more effective,⁶² while the orange band extends this region, taking into account the uncertainty coming from the chosen calculation level.⁶³ Inset pics represent the optimized structures of Au_{20} aggregates.

(which is the most stable form of Ag_{20} structures⁴⁷) presents the lowest T_1 levels. These levels span from 1.09 eV in the case of FACE defect, to 1.33 eV in the case of PURE cluster. The tetrahedral Au_{20} system shows the highest T_1 levels, with energies going from 1.76 eV (FACE case) to 2.23 eV (PURE case). The other two nanostructures behave in a mixed way, as expected. It is indeed reasonable (but not trivial) to expect that

the Au/Ag alloy and the Ag_{20} NC with a gold-like tetrahedral geometry ($\text{Ag}_{20}\text{-B}$) would have combined $\text{Au}_{20}/\text{Ag}_{20}\text{-A}$ electronic properties. This indicates that, beyond the chemical nature, the geometry of the aggregates has a prominent role in determining the energy levels distribution and thus the EET capabilities (the $\text{Ag}_{20}\text{-B}$ T_1 levels are more energetic compared to $\text{Ag}_{20}\text{-A}$ of 0.43 to 0.52 eV). However, not all possible geometries are equiprobable. We recovered that the $\text{Ag}_{20}\text{-B}$ form is less stable than $\text{Ag}_{20}\text{-A}$ of about 0.69 eV, indicating that in realistic conditions there would be a higher amount of $\text{Ag}_{20}\text{-A}$ than $\text{Ag}_{20}\text{-B}$.

Another interesting aspect that arises from [Figure 5](#) is related to the T_1 sensitivity toward the presence of matrix defects. If we compare the PURE and the defected cases (especially the FACE one), it is notable how here the presence of defects tends to decrease the energy of the T_1 level and that the magnitude of these downshifts is system-dependent. For example, while in $\text{Ag}_{20}\text{-A}$ the T_1 redshift between PURE and FACE is about 0.24 eV, in Au_{20} , this value is 0.44 eV. For $\text{Ag}_{20}\text{-B}$, the PURE to FACE T_1 energy difference is 0.33 eV, still larger than for $\text{Ag}_{20}\text{-A}$. The same trend can be recovered for the PURE versus TOP defected case, where the T_1 energy differences are 0.27, 0.19, and 0.25 eV for Au_{20} , $\text{Ag}_{20}\text{-A}$, and $\text{Ag}_{20}\text{-B}$, respectively. This indicates that, in general, the T_1 levels of Ag_{20} aggregates are less sensitive to the presence of matrix defects compared to the gold-based structure. The alloy behaves in an intermediate way (PURE vs FACE redshift of 0.37 eV and PURE vs TOP redshift of 0.24 eV), even when Ag and Au atoms are swapped and when the composition is changed from a 1:1 to a 1:4 Au/Ag ratio (see [Supporting Information](#) for detailed discussions). The fact that the same downshift trend is recovered for both defected cases indicates that this tendency does not depend on the location of the defect. Considering as the optimal energy interval for the EET the one represented by the green band in [Figure 5](#), it can be stated that $\text{Ag}_{20}\text{-A}$ always has the best T_1 energies, especially when defects are accounted, and this remains valid even if the underestimation (assumed to be of about 0.24 eV) given by the adopted XC-functional is taken into account.⁶³ As in the M_{12} case, we calculated the UV-vis absorption spectra of the investigated systems and reported them in [Figure 6](#). Within the wavelength of interest, $\text{Ag}_{20}\text{-B}$ has the highest absorption rate, followed by the $\text{Au}_{10}\text{Ag}_{10}$ alloy. This means that these two species would have the greatest excited states population and, thus, would have more chance to transfer the excitation to the Er^{3+} ions. $\text{Ag}_{20}\text{-A}$ and Au_{20} have similar absorption properties. Given the different features among $\text{Ag}_{20}\text{-A}$ and $\text{Ag}_{20}\text{-B}$, the geometry seems to play a major role. Considering only four model NCs is not enough to assess how the absorption cross-section depends on the system nature and geometry. In fact, given the experimental methods adopted to study such systems,^{19,22–26} in a real sample there would be several NC isomers whose population depends on the relative stability. Therefore, even if in these calculations gold seems a worse absorber than silver and the gold–silver alloy in the wavelength region considered, the theoretical results are not clear enough to conclude that this evidence can motivate the experimental observation of larger PL enhancement given by silver and alloyed NCs.^{22–24} To assess the role of matrix defects, we performed the same calculations on the optimized NC- H_3SiO_4^- TOP geometries. The absorption tendencies are similar to the ones reported in [Figure 6](#), although here we notice a general decrease in the absorbance intensities. This is

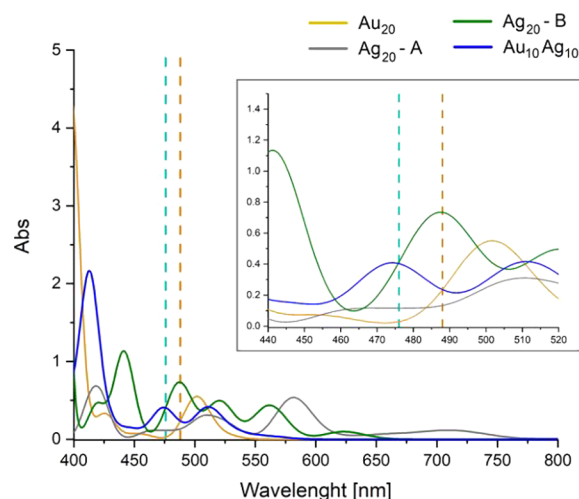


Figure 6. TDDFT-computed absorption spectra for the investigated M_{20} NCs. The inset shows a zoom over the 440–520 nm region. Light-blue and orange dashed lines represent the out-of-resonance (476 nm) and in-resonance (488 nm) wavelengths, respectively, which are commonly adopted to excite the systems in the experimental setups.^{19,22–26}

related to the presence of charge-transfer states between the anion and the NCs, which quench the optical absorption. More details are available in the [Supporting Information](#).

To summarize the findings presented in this paragraph, we found that, for M_{20} aggregates, silver-based systems have the best T_1 to $^4I_{13/2}$ Er^{3+} energy match. They may also exhibit an enhancement of the absorption cross-section in the relevant excitation window. Despite the nonoptimal T_1 levels distribution, the 1:1 Au/Ag alloy presents a remarkable absorption cross-section in the spectral region of interest. Finally, the gold-based structure resulted to have the worst energy level alignment toward the Er^{3+} accepting level and to be very sensitive to the presence of matrix defects; moreover, it has no intense absorption in the investigated wavelength region. However, such findings do not account for the hydrostatic effects the matrix has toward the NCs structures. The silica environment indeed naturally compresses the NCs geometries, shortening the bond lengths and affecting the electronic structures. In most cases such compression effect reflects into a slight T_1 level blueshift (as expected from the “particle in a box” model); however, in the case of Au_{20} the T_1 energy levels can be red-shifted by tenth of eV, thus, favoring the EET mechanism. A more extensive discussion on this point is given in the [Comparison with Experiments](#) section.

M_{58} ($M = \text{Au}, \text{Ag}$). The third group of NCs we investigated is the M_{58} ($M = \text{Au}, \text{Ag}$) family. Unlike the previous cases, here we did not perform evaluations on the alloy since there are no studies that investigate the equilibrium geometry of such large alloyed structure, and anyway, there are no experimental data on such systems to compare with. The calculated T_1 levels for Au_{58} and Ag_{58} are pictured in [Figure 7](#). Here the only defected form we could analyze is the TOP one since the spherical-like symmetry that characterizes the M_{58} does not allow to obtain a defined FACE configuration. Indeed, during the optimization procedure, the H_3SiO_4^- anion naturally moves in order to generate a bond with a metal atom. As visible from [Figure 7](#), all the calculated T_1 levels sit below the Er^{3+} emitting level and this makes the EET process forbidden. However, accounting for the possible T_1 levels underestimation given by the

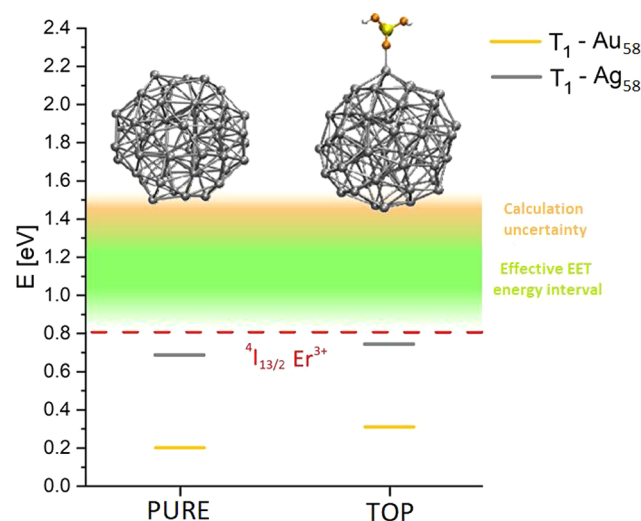


Figure 7. T_1 level distribution of the investigated M_{58} structures. The label PURE indicates results for the bare NCs, while TOP refers to a system where there is one matrix defect unit pointing toward a NCs edge. Red line represents the energy of $^4I_{13/2}$ Er^{3+} emitting level (0.81 eV).⁶¹ The green band indicates the region where the EET process is more effective,⁶² while the orange band extends this region taking into account the uncertainty coming from the chosen calculation level.⁶³ Inset pics represent the optimized structures of the Ag_{58} aggregates.

computational setup (see the discussion reported in the paragraph dedicated to M_{12}), the best match with the $^4I_{13/2}$ level seems to be given by the silver-based structure that presents T_1 levels at 0.69 and 0.74 eV for the PURE and TOP forms, respectively. If we consider an underestimation of about 0.24 eV, such energies increase to 0.93 and 0.98 eV, respectively, giving a nonzero probability of direct EET to the $^4I_{13/2}$ Er^{3+} level (0.81 eV), which would compete with the back-EET process. On the contrary, Au_{58} structure presents low-lying energy states whose energies are 0.20 and 0.33 eV for the PURE and TOP forms, respectively. Even accounting for errors introduced by the computational setup, these levels are too low to give an effective EET. Given the poor T_1 energy match and the complexity of the systems, we decided not to calculate the absorption spectrum of these species. Finally, we would like to remark that the computational protocol adopted in determining the M_{58} equilibrium structures was based on PM7 semiempirical algorithm rather than a DFT calculation. The minimum structures thus could be different from the DFT optimized ones and the optical properties can be affected by these structural differences. This is the case for silver and defected clusters, as we discuss in the [Supporting Information](#). However, despite the numerical differences, the physical considerations on the lower photoluminescence enhancing capabilities still remain valid at least for the bare Au_{58} and Ag_{58} clusters.

Role of the Relaxation of the Excited States Geometry. In the previous paragraphs, we discussed the results obtained through the application of linear-response TDDFT calculations on the DFT ground state optimized structures of the various noble-metal aggregates. Thus, the data we presented refer to vertical transitions. However, the contribution the excited states geometrical relaxation can have on the relative alignment of energy levels could be pivotal in understanding the different features the NCs have in the EET mechanism. The theoretical framework we are exploring

(the antenna–lanthanide paradigm) is based on the assumption that the EET occurs from the NCs T_1 levels to the Er^{3+} emitting level, due to the fact that triplet states are long-living states and therefore have more chance to transfer the excitation to the lanthanide. However, since these excited states can have a relatively long lifetime, their geometry can relax to the energy minimum before decaying to the ground state. In this view, the EET could take place at any time, from the moment the excited T_1 level is populated through intersystem crossing to the moment the NC reaches its T_1 excited state optimized geometry. When the EET occurs, the system relaxes instantaneously to the ground state, preserving the excited state geometrical configuration. This means that there is an energy interval in which the EET can occur, which goes from the energy of the $T_1 \rightarrow S_0$ transition calculated at the geometry of the ground state S_0 , to the energy of the $T_1 \rightarrow S_0$ transition, calculated at the equilibrium geometry of the excited state T_1 . We will now refer to these quantities as $\Delta E(q_{S_0})$ and $\Delta E(q_{T_1})$, where q_{S_0} and q_{T_1} indicate the equilibrium geometries of the ground state and of the first excited triplet state, respectively (see scheme in Figure 8). $\Delta E(q_{S_0})$ is exactly the

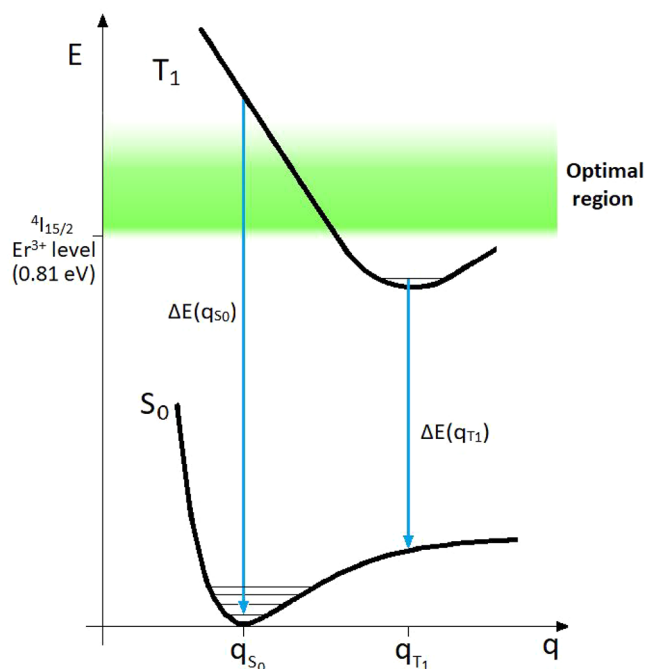


Figure 8. Qualitative representation of the T_1 and S_0 potential energy surfaces (black lines) with respect to the generic NCs geometry q . The green band represents a region where the EET process is more effective.

excitation energy that comes from the linear-response TDDFT calculations since it refers to the vertical transition computed assuming the geometry of the ground state. Then, we computed the T_1 equilibrium geometries for the M_{12} and M_{20} clusters and calculated the $\Delta E(q_{T_1})$ through a self-consistent field calculation, by imposing the proper spin multiplicity. $\Delta E(q_{S_0})$ and $\Delta E(q_{T_1})$ are collected in Table 1. We could not perform these calculations for the M_{58} cases because of the issues described in the Computational Methods.

In Table 1 we highlighted in bold the energies at which the EET could be effective, according to the criteria previously

Table 1. $\Delta E(q_{S_0})$ and $\Delta E(q_{T_1})$ for the M_{12} and M_{20} NCs^a

cluster	geometry	$\Delta E(q_{S_0})$ (eV)	$\Delta E(q_{T_1})$ (eV)
Au_{12}	PURE	1.17	0.52
	FACE	1.41	0.26
	TOP	1.31	0.29
Ag_{12}	PURE	0.89	0.54
	FACE	0.96	0.53
	TOP	0.99	0.26
Au_6Ag_6	PURE	0.95	0.46
	FACE	1.16	0.37
	TOP	1.06	0.26
Au_{20}	PURE	2.23	0.18
	FACE	1.79	1.26
	TOP	1.96	1.32
$\text{Ag}_{20}\text{-A}$	PURE	1.33	0.81
	FACE	1.09	0.83
	TOP	1.14	0.84
$\text{Ag}_{20}\text{-B}$	PURE	1.85	1.37
	FACE	1.52	0.57
	TOP	1.60	0.14
$\text{Au}_{10}\text{Ag}_{10}$	PURE	2.03	0.12
	FACE	1.66	0.69
	TOP	1.79	1.09

^aBold cells indicate the configurations where ΔE can lead to an effective EET process to the $^4I_{15/2}$ Er^{3+} level. In Figure 8 we schematized the role of the involved quantities.

discussed (see the paragraph dedicated to M_{12} results). In this treatment, we omitted a precise discussion on the effect the back-EET could have on the effectiveness of the EET process since it would certainly have a minor contribution compared to the one given by the excited state relaxation. Indeed, while the back-EET just decreases the probability of having an effective direct EET from the antenna to the lanthanide, the excited state relaxation can even suppress it. The data reported in Table 1 reveal that, if accounted for, the excited state relaxation can have a prominent role in these systems. Passing from q_{S_0} to q_{T_1} the energy difference always reduces as it should, but the decrement is strongly system-dependent. In particular, it can be seen how in all M_{12} NCs cases, when the equilibrium geometry of the first triplet excited state is reached, $\Delta E(q_{T_1})$ never allows the EET since its value is smaller than the $^4I_{13/2} \rightarrow ^4I_{15/2}$ Er^{3+} transition.

This means that with such small metal aggregates, the EET can effectively occur within a specific time frame from the moment the NCs reach its T_1 level. On the other hand, M_{20} presents different cases. $\text{Ag}_{20}\text{-A}$ always has its $\Delta E(q_{T_1})$ in a region where the EET is possible, even if its probability is compromised by the competition of the back-EET process ($\Delta E(q_{T_1}) \approx ^4I_{13/2}$). On the contrary, Au_{20} cluster never reaches an effective $\Delta E(q_{T_1})$ value, and thus has smaller EET rates. Considering the PURE form, its excited state energy falls way below the lanthanide accepting level ($\Delta E(q_{T_1}) = 0.18$ eV), meaning that the bare Au_{20}NC are capable to transfer its excitation only within a short time frame during the relaxation.

On the other hand, the defected forms present $\Delta E(q_{T_1})$ larger than the threshold assumed as reference for an effective EET process (1.24 eV). However, as reported in Table 1, the difference among the $\Delta E(q_{T_1})$ and this reference value is

minute, indicating a small but non-negligible EET probability. Due to this minute difference, such probability is certainly larger than the one calculated for EET acting the unrelaxed defected NC to lanthanide. Therefore, in this case, the presence of defects can enhance the EET yield upon geometry relaxation. The other M_{20} systems mostly behave like the PURE Au_{20} , with the exceptions of PURE Ag_{20} -B, whose case is more similar to the defected Au_{20} clusters, and of TOP $Au_{10}Ag_{10}$ form, where the relaxation brings the $\Delta E(q_{T_1})$ within the interval assumed for an effective EET. Globally, this analysis revealed that the intracuster dynamics associated with excited state relaxation can have an important effect on EET probability. In particular, we notice that, on average, relaxed M_{12} systems have less probability to transfer the excitation to the lanthanide compared to the M_{20} cases, even if they start from a proper $\Delta E(q_{S_0})$ energy. This is not always true in the case of M_{20} systems where the relaxation can sometimes bring the system within the eligible T_1 to $^4I_{13/2}$ transition range or in a closer region.

We can extend such observations to the M_{58} case by accounting that excited state relaxation always decreases the $T_1 \rightarrow S_0$ energy. As shown in Figure 7, for both the M_{58} structures, the T_1 levels sit below the Er^{3+} accepting level, and thus, the starting $\Delta E(q_{S_0})$ is already inadequate to give an effective EET to the lanthanide. If we account for the triplet state relaxation, the new $\Delta E(q_{T_1})$ would be smaller and thus the EET process would be even less likely.

■ COMPARISON WITH EXPERIMENTS

In this section, we will discuss the experimental results obtained on the enhanced lanthanide PL, in the perspective of the antenna–lanthanide paradigm. The computational results presented so far allowed to qualitatively determine the different performances the various NCs can have with respect to the Er^{3+} sensitization. On the basis of the various discussions reported in the previous sections, we can define four major criteria that a NC should meet in order to efficiently sensitize the lanthanide ions (the higher number of criteria met, the better the efficiency is expected to be):

1. Adequate $T_1(q_{S_0})$ to $^4I_{13/2}$ energy alignment.
2. During the relaxation, the $T_1(q)$ level has to cross the optimal EET region.
3. Adequate $T_1(q_{T_1})$ to $^4I_{13/2}$ energy alignment.
4. High absorption cross-section in the wavelength region of interest.

Indeed, an ideal NC antenna should have a proper T_1 to $^4I_{13/2}$ energy match in all stages of the excited states relaxation (first three criteria), as well as a high excited state population (fourth criterion). To summarize our findings, we classified in Table 2 the performance that analyzed M_{12} and M_{20} NCs have on the basis of these criteria. To ease the discussion, here we did not consider the role the back-EET can have on the process yield; we accounted for the features that affect the mere direct EET. As shown in Table 2, Ag and Au/Ag based NCs better match the criteria than the ones based on pure Au, both for the T_1 alignment and the absorbance rate. Regarding the differences among the NCs sizes, it can be noticed how the major difference resides in the T_1 energy location. If the relaxation is not accounted for, M_{12} presents the best levels alignment. However, when this effect is considered, none of

Table 2. Classification of the NCs Performances with Respect to the Requirements Specified in the Main Text^a

cluster	proper $T_1(q_{S_0}) - ^4I_{13/2}$ alignment	T_1 relaxation cross optimal EET region	proper $T_1(q_{T_1}) - ^4I_{13/2}$ alignment	high absorbance
Au_{12}	+	+++	–	++
Au_{20}	–	+	++*	+
Ag_{12}	+++	+++	–	+++
Ag_{20} -A	++	+++	+++	+
Ag_{20} -B	–	++	++*	+++
Au_6Ag_6	+++	+++	–	+
$Au_{10}Ag_{10}$	–	+++	+	++

^aWe give one plus symbol for each of the NCs configurations (PURE, FACE, and TOP) that satisfy the requirement. * indicates that the relaxed T_1 energy is located close to the optimal EET region upper limit (within 0.1 eV).

the relaxed M_{12} structures are able to support the EET, while many of the M_{20} could instead. Thus, the best performing NC size cannot be easily determined a priori. However, as shown in Table 2, M_{12} systems generally match slightly better the four criteria compared to the corresponding M_{20} structures. This is particularly apparent for Au, while for Ag and the mixed clusters, M_{12} and M_{20} have globally comparable results.

Before proceeding to the comparison with the experimental findings, we would like to underline that our theoretical approach is not expected to give quantitative prediction on these systems. In most of the experimental literature studies we are going to discuss, the metal ions were first incorporated by ion implantation and then, by controlling the annealing conditions, they nucleated and grew forming the NCs. Unfortunately, such complex conditions prevent an atomistic determination of the NCs sizes and geometries. For example, their characterization by Extended X-ray Absorption Fine Structure Spectroscopy (EXAFS) measurements generically assumed an average 3D compact shape. Obviously, this analysis cannot capture the high variety of geometrical configurations present in a realistic setup and return only a glimpse of the average effect this multitude of structures produce. Relying on the structural information given by EXAFS, our model NCs turn out to be representative of the mean NCs structures generated in the experiments, as shown by the geometrical comparison available in the Supporting Information. Even if such similarities do not ensure any correspondence between optoelectronic features of our model systems and the structure in the experimental system, our theoretical approach can explain many of the experimental findings and is able to predict new features on small Ag NCs which was experimentally observed for the first time. Thus, despite the limitations of our theoretical modeling, the resulting interpretation can be considered as a guide to further design effective NCs–lanthanide sensitizers.

Before starting to systematically present the comparisons, we would like to mention that we also performed an analysis aimed to investigate the effect the hydrostatic pressure of the dielectric matrix can have on the EET rates, by analyzing the T_1 energy of the various NCs when the mean bond lengths were shortened to exactly fit the experimental data. Such analysis reveals that in general, all compressed clusters' T_1 levels are slightly blue-shifted compared to the originals by a few hundredths of eV; therefore, this effect can be reasonably neglected. However, Au_{20} resulted to be more sensitive to the compression, since upon a proper rescaling of the mean bond

length (matching the compression factor of the Au₁₂ NCs), we found an energy redshift that brings the T_1 level to 1.85 eV, a value that is much closer to the optimal EET region.

Chemical Nature of the Clusters. The first point that arises from our results is that the excited states population and the optical absorption cross-section of the NCs strongly depend on the chemical nature of the system. In particular, we found that gold-based structures generally have worse levels alignments with respect to the Er³⁺ accepting level compared to Ag and the Au/Ag alloy systems. Moreover, we recall that the excited states relaxations of Ag structures preserve its ability to perform effective EET, as reported in Table 1. These effects combined can explain why in the experiments a larger PL enhancement is measured in the case of Ag and Au/Ag alloy compared to Au. As an example of these results, in Figure 1, we reported the trend as a function of the annealing temperature in a N₂ atmosphere of the Er³⁺ PL emission of three sets of Er-doped silica samples containing metallic nanoclusters of Au (orange dots), AuAg (blue dots), and Ag (red dots), incorporated by ion implantation.^{19,23,35} The legend shows the ratio of the Er/metal implantation fluence. At 600 °C (where the strongest PL emission is detected, featuring clusters with $N = 10$ – 15 atoms, as revealed by EXAFS),^{23,36} the Er³⁺ PL enhancement factor is about 17 for Ag, 15 for the Au/Ag alloy and 3 for the Au, as visible from Figure 1.⁶⁶ This trend agrees with the presented simulations. Considering clusters of a larger size, in ref 22, the authors reported the PL results of Er/Au coimplanted samples, for which EXAFS measurements revealed the presence of Au clusters of 25 atoms.^{22,36} The maximum PL enhancement factor was 6. Such moderate enhancement can be explained considering the role the defects have in determining the electronic properties of the systems. As discussed in the **Role of the Relaxation of the Excited States Geometry** paragraph, Au₂₀ defected systems are affected by an excited states relaxation that decreases the $T_1 \rightarrow S_0$ energy gap, bringing it into a region where the EET probability is small but non-negligible and thus increasing the whole EET rate. Notice that, in this view, matrix defects play a major role in determining the EET probability toward Er³⁺ ions.

In ref 24, the PL results of Er/Ag coimplanted samples were reported and a much stronger maximum PL enhancement factor of 25 was demonstrated. This value is even larger than the factor 17 obtained for the samples in Figure 1, in agreement with the results of the simulations presented here which indicate the Ag₂₀-A as the most effective configuration for the EET (the implantation fluency ratio adopted in Figure 1 should provide $N \approx 10$ – 15 atoms, while the one used in ref 24 should generate larger aggregates of $N \approx 20$ – 25 atoms, based on Au results). Moreover, in a work by Eichelbaum et al., it was found that the Eu³⁺ PL can be effectively enhanced by 250× when small silver aggregates are present, while in the presence of gold aggregates the enhancement factor is only about 5.²¹ We remark that this large difference is also motivated by the different concentrations that could be achieved for the two metals in the silica matrix (370 ppm for Ag vs 50 ppm for gold). Yet, also taking this concentration ratio into account, silver turns out to intrinsically be a better sensitizer compared to gold, in line with our computational findings.

Size Dependence of the Enhancement. Regarding the size dependence, in the case of Au clusters, in ref 19 it was reported a detailed study of the Er³⁺ PL emission of samples

implanted with Au at different fluences and thermally treated in a N₂ atmosphere, which demonstrated an increase (and a shift toward higher temperatures) in the maximum PL enhancement for decreasing Au implantation fluences and thus for a decreasing average size of the Au clusters, as measured by EXAFS.³⁶ This trend is consistent with our computational findings, which show a shift of the T_1 level toward the optimal band for EET going from Au₂₀ to Au₁₂ (see Figures 5 and 3). Moreover, this agrees with the considerations made above on Table 2. Conversely, in the case of larger clusters, it was demonstrated experimentally that for sizes in the range of 50–60 atoms the enhancement is suppressed.^{22–24} Again, this is in line with the simulation results reported for the M₅₈ clusters (Figure 7). It is worth underlining that the proposed mechanism may also be relevant for systems involving different lanthanides, such as the case of Dy³⁺ ions. In a work by Jiménez et al. it was noticed how the presence of silver nanoparticles with the diameter of about 2 nm can suppress the Dy³⁺ emission ($^4F_{9/2} \rightarrow ^6H_{15/2}$ at 484 nm and the $^4F_{9/2} \rightarrow ^6H_{13/2}$ at 574 nm transitions) as the nanoparticle concentration increases.⁶⁷ The main reason was identified to be an “ion-to-particle excitation energy transfer operating via surface plasmons in the nanoscale metal.” In addition to such effect, we propose that due to the large size of the silver nanoparticles, the antenna T_1 levels are too low in energy to support an effective particle-to-ion EET. Thus, the antenna–lanthanide effect cannot take place, and the Dy³⁺ emission does not benefit from it.

Role of the Excitation Wavelength. Connected to the optical absorption cross-section of the various NCs, the computational results also provide a possible justification of why lower experimental excitation wavelengths give higher Er³⁺PL enhancing factor.²² As shown in Figures 4 and 6, the lower the excitation wavelength is the more intense the optical absorption peaks are. Thus, the more energetic is the incoming radiation, the higher is the NCs excited states population and the more excitations can be transferred to the lanthanide, resulting in an enhanced PL.

Effect of Annealing in a Reducing Atmosphere. Notably, the theoretical framework we are proposing allows to explain and predict the effect a reducing atmosphere annealing can have on the lanthanide PL. It was observed in ref 37 that small Au_N aggregates ($N = 5$ – 10) can increase the Er³⁺ PL more effectively when the samples are annealed in a reducing atmosphere compared to the ones annealed in an inert atmosphere.³⁷ We can explain this effect as follows. Reducing atmosphere can significantly decrease the number of defects in the matrix by reducing the dangling bonds of silica. Based on the computational results presented for the Au₁₂ clusters, decreasing the number of defects would reduce the spread of the energy band in which the T_1 levels can be located, focusing the T_1 potential energy surface within the region where the EET to Er³⁺ is more effective (see the PURE Au₁₂ system, data in Table 1). In the same way we can explain why the PL enhancement is reduced in Au_N systems ($N = 20$ – 25) when annealed in a reducing atmosphere.²² As discussed, the presence of defects plays a beneficial role in determining the Au₂₀ PL capabilities. When the sample is annealed in a reducing atmosphere, there are bonds saturations that prevent such beneficial role to take place. Finally, the same framework can be used to interpret the results of new PL measurements performed on Er–Ag coimplanted silica samples thermally treated in reducing atmosphere. In Figure 9 we report the

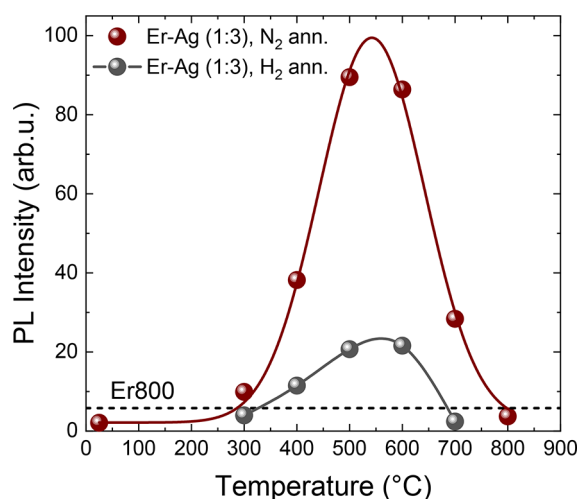


Figure 9. PL intensity at 1540 nm as a function of the annealing temperature of Er–Ag coimplanted silica samples. Red dots indicate the results of the samples annealed in inert (N_2) atmosphere. Gray dots are the results of the samples annealed in reducing ($Ar + H_2$) atmosphere. The solid lines are to be used as a guide for the eye. The black dashed line indicates the PL emission intensity of the reference sample (Er800). The PL measurements have been taken with resonant excitation at 488 nm.

trend, as a function of the annealing temperature, of the Er^{3+} PL emission of the samples annealed in inert atmosphere (N_2 , red dots) and reducing atmosphere ($Ar + H_2$, gray dots). Details on the experimental conditions used to produce the samples and perform PL measurements are reported in the [Experimental Methods](#). The implantation conditions are the same of the samples reported in [Figure 1](#).

A maximum PL enhancement factor of 4 is obtained when the reducing atmosphere is used with respect to the factor 17 obtained for annealing in inert atmosphere. Considering the computational results shown in [Figure 3](#) and [Table 1](#), we can observe that, differently from the Au_{12} case, the Ag_{12} PURE system has a T_1 level located very close to the bottom edge of the effective EET energy region. Here the back-energy transfer can be highly competitive with the direct process. Thus, even the small T_1 level increase given by the defects can have a favorable impact leading to PL enhancement. In this case thus a passivation of the defects has a detrimental effect on the effectiveness of EET, decreasing the PL enhancement, as shown in [Figure 9](#). As a final comment, it has to be noted that in principle the size of the NCs may be slightly different in the two annealing atmospheres, as evidenced in [ref 22](#), due to the different effective diffusion coefficient of the metal atoms as a function of the annealing atmosphere. This could explain the larger sensitivity of the PL results on the passivation of the surface defects compared to what can be qualitatively predict by the calculations.

CONCLUSIONS

In this work we investigated lanthanide (Er^{3+}) sensitization by metal nanoclusters in light of the antenna–lanthanide paradigm (used so far for lanthanide sensitization by organic ligands). We thus considered the enhanced lanthanide emission as a consequence of an energy transfer process that involves the nanoclusters first excited triplet state (which is the longest living excited state) and the lanthanide-emitting level. To test this hypothesis, we studied the energy levels

distribution and the absorption properties of several model nanoclusters which vary in size, geometry, and composition by means of TDDFT. In these calculations the presence of matrix defects was accounted through a simple model. We focused on silica-matrix implanted Er^{3+} ions, because of the widespread technological interest of this system and the availability of experimental data.^{16,18,22–24} Given a nanostructure, we defined different aspects that can regulate the performance of the energy transfer process, namely, the level alignment with the Er^{3+} accepting level and its dependency on the excited states relaxation and the optical absorption cross-section. Our calculations suggest that the enhancement is generally more effective when the nanoclusters are composed by Ag atoms or by a mixture of Au and Ag atoms, while the worst performances were obtained by Au-based structures. Moreover, the 12 atoms structures resulted to satisfy the aforementioned criteria more effectively than larger NCs, presenting, in particular, a more adequate T_1 energy alignment. All these considerations are in line with the available experimental data. We were further able to rationalize the nonobvious effect a reducing atmosphere annealing can have on these systems. We indeed proposed that such reducing atmosphere can saturate the matrix dangling bonds, with the effect of decreasing the number of defects. In turn, defects may be detrimental or beneficial for PL, depending on the exact system considered (chemical composition and size). This can explain why reducing annealing conditions enhance the Er^{3+} emission yield when sensitized by small Au nanoclusters, while they are detrimental in the case of Ag NCs, as confirmed by novel experimental measures reported here for the first time. The same considerations applied to the case of Au_{20} revealed that the silica-matrix defects can actively take part in the EET mechanism by modifying the NCs excited states distribution, and, in some cases, are beneficial for the whole process yield. Globally, our theoretical approach was able to qualitatively rationalize the experimental findings, by using the unifying character of the antenna–lanthanide paradigm. As such, this approach can be taken as a guide to design new and more effective rare-earth ions sensitizers based on metal clusters.

ASSOCIATED CONTENT

Supporting Information

The Supporting Information is available free of charge at <https://pubs.acs.org/doi/10.1021/acsphotonics.0c01884>.

Energy levels distribution of swapped structures; Calculations on M_{12} structural isomers; Investigation of the Au_4Ag_{16} nanoalloy; Cohesive energy analysis; TDDFT calculations on PM7 optimized structures; Absorption spectra of defected systems; Mulliken population analysis; Results obtained with CAM-B3LYP functional; Geometrical comparison with the experimental data (PDF)

AUTHOR INFORMATION

Corresponding Authors

Stefano Corni – Department of Chemical Sciences, University of Padova, 35131 Padova, Italy; CNR Institute of Nanoscience, 41125 Modena, Italy; orcid.org/0000-0001-6707-108X; Email: stefano.corni@unipd.it

Tiziana Cesca – Department of Physics and Astronomy, University of Padova, 35131 Padova, Italy; orcid.org/0000-0002-7102-6860; Email: tiziana.cesca@unipd.it

Authors

Mirko Vanzan – Department of Chemical Sciences, University of Padova, 35131 Padova, Italy; orcid.org/0000-0003-3521-8045

Boris Kalinic – Department of Physics and Astronomy, University of Padova, 35131 Padova, Italy; orcid.org/0000-0003-1750-4929

Chiara Maurizio – Department of Physics and Astronomy, University of Padova, 35131 Padova, Italy; orcid.org/0000-0002-0517-1314

Giovanni Mattei – Department of Physics and Astronomy, University of Padova, 35131 Padova, Italy

Complete contact information is available at:

<https://pubs.acs.org/10.1021/acsphotonics.0c01884>

Author Contributions

The manuscript was written through contributions of all authors. All authors have given approval to the final version of the manuscript.

Notes

The authors declare no competing financial interest.

ACKNOWLEDGMENTS

M.V. and S.C. thank MIUR-FARE for funding under the Grant Plasmochem.

REFERENCES

- (1) Bünzli, J. C. G.; Piguet, C. Taking Advantage of Luminescent Lanthanide Ions. *Chem. Soc. Rev.* **2005**, *34* (12), 1048–1077.
- (2) Eliseeva, S. V.; Bünzli, J. C. G. Lanthanide Luminescence for Functional Materials and Bio-Sciences. *Chem. Soc. Rev.* **2010**, *39* (1), 189–227.
- (3) Binnemans, K. Lanthanide-Based Luminescent Hybrid Materials. *Chem. Rev.* **2009**, *109* (9), 4283–4374.
- (4) Martucci, A.; De Nuntis, M.; Ribaudo, A.; Guglielmi, M.; Padovani, S.; Enrichi, F.; Mattei, G.; Mazzoldi, P.; Sada, C.; Trave, E.; Battaglin, G.; Gonella, F.; Borsella, E.; Falconieri, M.; Patrini, M.; Fick, J. Silver-Sensitized Erbium-Doped Ion-Exchanged Sol-Gel Waveguides. *Appl. Phys. A: Mater. Sci. Process.* **2005**, *80* (3), 557–563.
- (5) Wang, W. C.; Zhou, B.; Xu, S. H.; Yang, Z. M.; Zhang, Q. Y. Recent Advances in Soft Optical Glass Fiber and Fiber Lasers. *Prog. Mater. Sci.* **2019**, *101*, 90–171.
- (6) Qiao, J.; Zhao, J.; Liu, Q.; Xia, Z. Recent Advances in Solid-State LED Phosphors with Thermally Stable Luminescence. *J. Rare Earths* **2019**, *37* (6), 565–572.
- (7) Becker, P. C.; Olsson, N. A.; Simpson, J. R. Erbium-Doped Fiber Amplifiers: Photonic Crystal Fibers. *Materials Science*; Springer, 1999, Vol. 102, pp 203–218, DOI: 10.1007/978-1-4020-6326-8_6.
- (8) Saglamyurek, E.; Jin, J.; Verma, V. B.; Shaw, M. D.; Marsili, F.; Nam, S. W.; Oblak, D.; Tittel, W. Quantum Storage of Entangled Telecom-Wavelength Photons in an Erbium-Doped Optical Fibre. *Nat. Photonics* **2015**, *9* (2), 83–87.
- (9) Polman, A. Erbium as a Probe of Everything? *Phys. B* **2001**, *300*, 78–90.
- (10) Snoeks, E.; Kik, P. G.; Polman, A. Concentration Quenching in Erbium Implanted Alkali Silicate Glasses. *Opt. Mater.* **1996**, *5*, 159–167.
- (11) Hehlen, M. P.; Cockroft, N. J.; Gosnell, T.; Bruce, A. J. Spectroscopic Properties Of- and-Doped Soda-Lime Silicate and Aluminosilicate Glasses. *Phys. Rev. B: Condens. Matter Mater. Phys.* **1997**, *56* (15), 9302–9318.
- (12) Strohhofer, C.; Polman, A. Absorption and Emission Spectroscopy in Er³⁺ - Yb³⁺ Doped Aluminum Oxide Waveguides. *Opt. Mater.* **2003**, *21*, 705–712.
- (13) Kik, P. G.; Brongersma, M. L.; Polman, A. Strong Exciton-Erbium Coupling in Si Nanocrystal-Doped SiO₂. *Appl. Phys. Lett.* **2000**, *76* (17), 2325–2327.
- (14) Pacifici, D.; Franzò, G.; Priolo, F.; Iacona, F.; Dal Negro, L. Modeling and Perspectives of the Si Nanocrystals-Er Interaction for Optical Amplification. *Phys. Rev. B: Condens. Matter Mater. Phys.* **2003**, *67*, 245301.
- (15) Michieli, N.; Kalinic, B.; Scian, C.; Cesca, T.; Mattei, G. Emission Rate Modification and Quantum Efficiency Enhancement of Er³⁺ Emitters by Near-Field Coupling with Nanohole Arrays. *ACS Photonics* **2018**, *5* (6), 2189–2199.
- (16) Fares, H.; Elhouichet, H.; Gelloz, B.; Férid, M. Surface Plasmon Resonance Induced Er³⁺ Photoluminescence Enhancement in Tellurite Glass. *J. Appl. Phys.* **2015**, *117*, 193102.
- (17) Trave, E.; Mattei, G.; Mazzoldi, P.; Pellegrini, G.; Scian, C.; Maurizio, C.; Battaglin, G. Sub-Nanometric Metallic Au Clusters as Efficient Er³⁺ Sensitizers in Silica. *Appl. Phys. Lett.* **2006**, *89*, 151121.
- (18) Mattarelli, M.; Montagna, M.; Vishnubhatla, K.; Chiasera, A.; Ferrari, M.; Righini, G. C. Mechanisms of Ag to Er Energy Transfer in Silicate Glasses: A Photoluminescence Study. *Phys. Rev. B: Condens. Matter Mater. Phys.* **2007**, *75*, 125102.
- (19) Cesca, T.; Kalinic, B.; Maurizio, C.; Scian, C.; Battaglin, G.; Mazzoldi, P.; Mattei, G. Interatomic Coupling of Au Molecular Clusters and Er³⁺ Ions in Silica. *ACS Photonics* **2015**, *2*, 96–104.
- (20) Cesca, T.; Maurizio, C.; Kalinic, B.; Perotto, G.; Mazzoldi, P.; Trave, E.; Battaglin, G.; Mattei, G. Implantation Damage Effects on the Er³⁺ Luminescence in Silica. *Opt. Express* **2012**, *20* (15), 16639.
- (21) Eichelbaum, M.; Rademann, K. Plasmonic Enhancement or Energy Transfer? On the Luminescence of Gold-, Silver-, and Lanthanide-Doped Silicate Glasses and Its Potential for Light-Emitting Devices. *Adv. Funct. Mater.* **2009**, *19* (13), 2045–2052.
- (22) Maurizio, C.; Trave, E.; Perotto, G.; Bello, V.; Pasqualini, D.; Mazzoldi, P.; Battaglin, G.; Cesca, T.; Scian, C.; Mattei, G. Enhancement of the Er³⁺ Luminescence in Er-Doped Silica by Few-Atom Metal Aggregates. *Phys. Rev. B: Condens. Matter Mater. Phys.* **2011**, *83*, 195430.
- (23) Cesca, T.; Kalinic, B.; Michieli, N.; Maurizio, C.; Trapananti, A.; Scian, C.; Battaglin, G.; Mazzoldi, P.; Mattei, G. Au-Ag Nanoalloy Molecule-like Clusters for Enhanced Quantum Efficiency Emission of Er³⁺ Ions in Silica. *Phys. Chem. Chem. Phys.* **2015**, *17* (42), 28262–28269.
- (24) Trave, E.; Back, M.; Cattaruzza, E.; Gonella, F.; Enrichi, F.; Cesca, T.; Kalinic, B.; Scian, C.; Bello, V.; Maurizio, C.; Mattei, G. Control of Silver Clustering for Broadband Er³⁺ Luminescence Sensitization in Er and Ag Co-Implanted Silica. *J. Lumin.* **2018**, *197*, 104–111.
- (25) Cesca, T.; Kalinic, B.; Michieli, N.; Maurizio, C.; Scian, C.; Devaraju, G.; Battaglin, G.; Mazzoldi, P.; Mattei, G. Energy-Transfer from Ultra-Small Au Nanoclusters to Er³⁺ Ions: A Short-Range Mechanism. *Phys. Chem. Chem. Phys.* **2014**, *16* (29), 15158–15163.
- (26) Cesca, T.; Kalinic, B.; Maurizio, C.; Scian, C.; Battaglin, G.; Mazzoldi, P.; Mattei, G. Near-Infrared Room Temperature Luminescence of Few-Atom Au Aggregates in Silica: A Path for the Energy-Transfer to Er³⁺ Ions. *Nanoscale* **2014**, *6* (3), 1716–1724.
- (27) Hasegawa, Y.; Kitagawa, Y.; Nakanishi, T. Effective Photosensitized, Electrosensitized, and Mechanosensitized Luminescence of Lanthanide Complexes. *NPG Asia Mater.* **2018**, *10* (4), 52–70.
- (28) Bünzli, J. C. G.; Eliseeva, S. V. *Basics of Lanthanide Photophysics*; EPFL, 2010, DOI: 10.1007/4243.
- (29) Kawawaki, T.; Negishi, Y.; Kawasaki, H. Photo/Electrocatalysis and Photosensitization Using Metal Nanoclusters for Green Energy and Medical Applications. *Nanoscale Adv.* **2020**, *2* (1), 17–36.
- (30) The direct T₁ to ⁴I_{13/2} EET is not the only process that can populate the Er³⁺ emitting level. There can be other competitive mechanisms (e.g., direct Er³⁺ light absorption, EET from a NC singlet excited state, etc.) that populate the higher energy states of the lanthanide that further relax to the emitting level. However, since T₁ is the longest-living antenna excited state, EET would mainly start from this level.²⁸ Thus, to rationalize the EET process, it is reasonable to

start analyzing the energy of NCs T_1 state with respect to the $^4I_{13/2}$ Er^{3+} emitting level.

(31) Velázquez, J. J.; Tikhomirov, V. K.; Chibotaru, L. F.; Cuong, N. T.; Kuznetsov, A. S.; Rodríguez, V. D.; Nguyen, M. T.; Moshchalkov, V. V. Energy Level Diagram and Kinetics of Luminescence of Ag Nanoclusters Dispersed in a Glass Host. *Opt. Express* **2012**, *20* (12), 13582–13591.

(32) Kuznetsov, A. S.; Velázquez, J. J.; Tikhomirov, V. K.; Mendez-Ramos, J.; Moshchalkov, V. V. Quantum Yield of Luminescence of Ag Nanoclusters Dispersed within Transparent Bulk Glass vs. Glass Composition and Temperature. *Appl. Phys. Lett.* **2012**, *101*, 251106.

(33) Cuong, N. T.; Tikhomirov, V. K.; Chibotaru, L. F.; Stesmans, A.; Rodríguez, V. D.; Nguyen, M. T.; Moshchalkov, V. V. Experiment and Theoretical Modeling of the Luminescence of Silver Nanoclusters Dispersed in Oxyfluoride Glass. *J. Chem. Phys.* **2012**, *136*, 174108.

(34) Marian, C. M. Spin-Orbit Coupling and Intersystem Crossing in Molecules. *Comput. Mol. Sci.* **2012**, *2*, 187–203.

(35) Kalinic, B.; Cesca, T.; Scian, C.; Michieli, N.; Balasa, I. G.; Trave, E.; Mattei, G. Emission Efficiency Enhancement of Er^{3+} Ions in Silica by Near-Field Coupling With Plasmonic and Pre-Plasmonic Nanostructures. *Phys. Status Solidi A* **2018**, *215*, 1700437.

(36) Maurizio, C.; Cesca, T.; Perotto, G.; Kalinic, B.; Michieli, N.; Scian, C.; Joly, Y.; Battaglin, G.; Mazzoldi, P.; Mattei, G. Core-Shell-like Au Sub-Nanometer Clusters in Er-Implanted Silica. *Nanoscale* **2015**, *7* (19), 8968–8977.

(37) Cesca, T.; Kalinic, B.; Maurizio, C.; Michieli, N.; Scian, C.; Mattei, G. Amplified Sensitization of Er^{3+} Luminescence in Silica by Au Nanoclusters upon Annealing in a Reducing Atmosphere. *RSC Adv.* **2016**, *6* (101), 99376–99384.

(38) Kang, X.; Li, Y.; Zhu, M.; Jin, R. Atomically Precise Alloy Nanoclusters: Syntheses, Structures, and Properties. *Chem. Soc. Rev.* **2020**, *49* (17), 6443–6514.

(39) Jin, R. Atomically Precise Metal Nanoclusters: Stable Sizes and Optical Properties. *Nanoscale* **2015**, *7* (5), 1549–1565.

(40) Lu, Y.; Chen, W. Sub-Nanometre Sized Metal Clusters: From Synthetic Challenges to the Unique Property Discoveries. *Chem. Soc. Rev.* **2012**, *41* (9), 3594–3623.

(41) Chakraborty, I.; Pradeep, T. Atomically Precise Clusters of Noble Metals: Emerging Link between Atoms and Nanoparticles. *Chem. Rev.* **2017**, *117* (12), 8208–8271.

(42) Baleto, F. Structural Properties of Sub-Nanometer Metallic Clusters. *J. Phys.: Condens. Matter* **2019**, *31*, 113001.

(43) Li, J.; Li, X.; Zhai, H. J.; Wang, L. S. Au_{20} : A Tetrahedral Cluster. *Science* **2003**, *299* (5608), 864–867.

(44) Baleto, F.; Ferrando, R. Doped Golden Fullerene Cages. *Phys. Chem. Chem. Phys.* **2015**, *17* (42), 28256–28261.

(45) McKee, M. L.; Samokhvalov, A. Density Functional Study of Neutral and Charged Silver Clusters Ag_n with $n = 2–22$. Evolution of Properties and Structure. *J. Phys. Chem. A* **2017**, *121* (26), 5018–5028.

(46) Hong, L.; Wang, H.; Cheng, J.; Huang, X.; Sai, L.; Zhao, J. Atomic Structures and Electronic Properties of Small Au-Ag Binary Clusters: Effects of Size and Composition. *Comput. Theor. Chem.* **2012**, *993*, 36–44.

(47) Nhat, P. V.; Tai, T. B. Electronic Structure of Coinage Metal Clusters M_{20} ($M = Cu, Ag, Au$) from Density Functional Calculations and the Phenomenological Shell Model. *Chem. Phys. Lett.* **2018**, *706*, 127–132.

(48) Takenaka, M.; Hashimoto, Y.; Iwasa, T.; Taketsugu, T.; Seniutinas, G.; Balčytis, A.; Juodkakis, S.; Nishijima, Y. First Principles Calculations Toward Understanding SERS of 2,2'-Bipyridyl Adsorbed on Au, Ag, and Au-Ag Nanoalloy. *J. Comput. Chem.* **2019**, *40* (8), 925–932.

(49) Ouyang, R.; Xie, Y.; Jiang, D. E. Global Minimization of Gold Clusters by Combining Neural Network Potentials and the Basin-Hopping Method. *Nanoscale* **2015**, *7* (36), 14817–14821.

(50) Chaves, A. S.; Piotrowski, M. J.; Da Silva, J. L. F. Evolution of the Structural, Energetic, and Electronic Properties of the 3d, 4d, and 5d Transition-Metal Clusters (30 TM_n Systems for $n = 2–15$): A

Density Functional Theory Investigation. *Phys. Chem. Chem. Phys.* **2017**, *19* (23), 15484–15502.

(51) Hay, P. J.; Wadt, W. R. Ab Initio Effective Core Potentials for Molecular Calculations. Potentials for the Transition Metal Atoms Sc to Hg. *J. Chem. Phys.* **1985**, *82* (1), 270–283.

(52) Lugo, G.; Schwanen, V.; Fresch, B.; Remacle, F. Charge Redistribution Effects on the UV-Vis Spectra of Small Ligated Gold Clusters: A Computational Study. *J. Phys. Chem. C* **2015**, *119* (20), 10969–10980.

(53) Azarias, C.; Adamo, C.; Perrier, A. Modeling the Photosensitizing Properties of Thiolate-Protected Gold Nanoclusters. *Phys. Chem. Chem. Phys.* **2016**, *18* (11), 7737–7750.

(54) Agrachev, M.; Antonello, S.; Dainese, T.; Gascón, J. A.; Pan, F.; Rissanen, K.; Ruzzi, M.; Venzo, A.; Zoleo, A.; Maran, F. A Magnetic Look into the Protecting Layer of Au_{25} Clusters. *Chem. Sci.* **2016**, *7*, 6910–6918.

(55) Vanzan, M.; Corni, S. Role of Organic Ligands Orientation on the Geometrical and Optical Properties of $Au_{25}(SCH_3)_{18}^0$. *J. Phys. Chem. A* **2018**, *122* (34), 6864–6872.

(56) Mato, J.; Guidez, E. B. Accuracy of the PM6 and PM7 Methods on Bare and Thiolate-Protected Gold Nanoclusters. *J. Phys. Chem. A* **2020**, *124* (13), 2601–2615.

(57) Frisch, M. J.; Trucks, G. W.; Schlegel, H. B.; Scuseria, G. E.; Robb, M. A.; Cheeseman, J. R.; Scalmani, G.; Barone, V.; Petersson, G. A.; Nakatsuji, H.; Li, X.; Caricato, M.; Marenich, A.; Bloino, J.; Janesko, B. G.; Gomperts, R.; Mennucci, B.; Hratchian, H. P.; Ortiz, J. V.; Izma, A. F.; Fox, D. J., et al. *Gaussian 09*, Revision B.01; Gaussian, Inc: Wallingford, CT, 2010.

(58) O'Boyle, N. M.; Tenderholt, A. L.; Langner, K. M. Cclib: A Library for Package-Independent Computational Chemistry Algorithms. *J. Comput. Chem.* **2008**, *29*, 839–845.

(59) Tomasi, J.; Mennucci, B.; Cammi, R. Quantum Mechanical Continuum Solvation Models. *Chem. Rev.* **2005**, *105* (8), 2999–3093.

(60) Lide, D. R.; Haynes, W. M. M.; Baysinger, G.; Berger, L. I.; Kehiaian, H. V.; Roth, D. L.; Zwillinger, D.; Frenkel, M.; Goldberg, R. N. *CRC Handbook of Chemistry and Physics*; CRC Press, 2010.

(61) Polman, A. Erbium Implanted Thin Film Photonic Materials. *J. Appl. Phys.* **1997**, *82* (1), 1–39.

(62) Latva, M.; Takalo, H.; Mukkala, V. M.; Matachescu, C.; Rodríguez-Ubis, J. C.; Kankare, J. Correlation between the Lowest Triplet State Energy Level of the Ligand and Lanthanide(III) Luminescence Quantum Yield. *J. Lumin.* **1997**, *75* (2), 149–169.

(63) Leang, S. S.; Zahariev, F.; Gordon, M. S. Benchmarking the Performance of Time-Dependent Density Functional Methods. *J. Chem. Phys.* **2012**, *136*, 104101.

(64) Boyd, K.; Ebendorff-Heidepriem, H.; Monro, T. M.; Munch, J. Surface Tension and Viscosity Measurement of Optical Glasses Using a Scanning CO_2 Laser. *Opt. Mater. Express* **2012**, *2* (8), 1101–1110.

(65) Such estimations were obtained through calculations performed on a wide set of organic molecules whose chemical nature is different compared to the present metal NCs. However, as far as we know, an extensive TDDFT benchmark study on the excited state properties of metal-based nanostructures is lacking to date, and using the existing benchmark is the best option.

(66) For the Ag case, preliminary EXAFS measurements give $n = 8$ atoms and a distance $d_{Ag-Ag} = 2.73$ Å.

(67) Jiménez, J. A. Influence of Ag Nanoparticles on the Luminescence Dynamics of Dy^{3+} Ions in Glass: The “Plasmonic Diluent” Effect. *Phys. Chem. Chem. Phys.* **2013**, *15* (40), 17587–17594.